INTERNATIONAL JOURNAL FOR NUMERICAL METHODS IN FLUIDS, VOL. 17, 365–384 (1993)

A PARABOLIC NUMERICAL PROCEDURE FOR THREE-DIMENSIONAL VISCOUS ROTATING FLOWS

QINGPING SHI*

Department of Mechanical, Aerospace and Nuclear Engineering, University of Virginia, Charlottesville, VA 22903-2442, U.S.A.

AND

R. J. RIBANDO†

Department of Mechanical, Aerospace and Nuclear Engineering, University of Virginia, Charlottesville, VA 22903-2442, U.S.A.

SUMMARY

This paper presents the development of a parabolic numerical procedure for rotating flows and its applications to three-dimensional viscous rotating flows. The formulation is based on the Navier–Stokes equations in general co-ordinates fixed on a rotating frame, so that the rotation effect is included in the guess-correct process. The use of body-fitted curvilinear co-ordinates makes it easier to handle the complex geometries of turbomachinery components. In the present work a k–ε turbulence model was used for the three-dimensional numerical tests. The algorithm is equally applicable to incompressible and compressible flows. Comparisons of the predicted results with the experimental data were reasonably good, and the solutions were stable to rotational speeds up to at least 14 000 rpm.

KEY WORDS Turbomachinery Rotating Parabolic Body-fitted co-ordinates

INTRODUCTION

Over the past several decades much effort has been devoted to developing accurate and efficient numerical algorithms suitable for predicting the flow fields in turbomachinery. Earlier work usually began with the assumption of inviscid flow, which made it much easier and solvable without the help of modern computers. Reviews of the inviscid flow simulations can be found in several articles.[1–3] One of the biggest drawbacks is that inviscid models fail to predict some important phenomena of rotating flows, such as secondary flows and jet/wake throughflow patterns.

A number of viscous flow simulations of rotating channels[4–6] as well as centrifugal impellers[7–9] have been reported. Most of them are based on the solution of parabolized Navier–Stokes equations and a parabolic numerical procedure. Several researchers[4–6] applied the parabolic numerical procedure known as the SIMPLE algorithm[10] to the numerical simulations of rotating

---

* Graduate Research Assistant.

† Lucien Carr III Associate Professor of Engineering Education.

0271–2091/93/170365–20$15.00

Received September 1992
Revised January 1993

flows. However, the method failed to predict rotating flow fields at high rotation speed. The reason is that the Coriolis force is important for generating some distinct flow phenomena such as secondary flows and jet/wake flow patterns. The original parabolic numerical procedure does not explicitly include its influence in the guess-correct process.

Recently the authors[11] reported a new pressure-based numerical procedure as well as its application to two-dimensional rotating flow computations. The numerical procedure was inspired by the generalized pressure-based numerical procedures proposed by Rhie[12] and Peric,[13] and includes the effect of rotation from the very beginning of the derivation. However, most rotating flows are three-dimensional in nature, and some flow phenomena such as secondary flows cannot be predicted with two-dimensional flow calculations. In the present work a general form of the parabolic numerical procedure for three-dimensional (3D) rotating flows is developed. This paper presents a description of the procedure and compares the numerical results with experimental results for the rotating flows tested by Eckardt,[14,15] and Wagner and Velkoff.[16]

GOVERNING EQUATIONS

In the present research, a body-fitted curvilinear co-ordinate system is used to handle the geometrical complexity common to turbomachinery components. There are various ways to derive the governing equations in curvilinear co-ordinates. In order to have the strong conservation form of the differential equations, the Cartesian base vectors are employed as a fixed basis, i.e. Cartesian components of vectors and tensors are used. Therefore, it is convenient to transform the governing equations from the Cartesian co-ordinate system to a general co-ordinate system. The time-averaged governing equations in Cartesian co-ordinates in a rotating reference frame are written as

$$\frac{\partial(\rho u_j)}{\partial x_j}=0\,, \tag{1}$$

$$\frac{\partial(\rho u_i u_j)}{\partial x_j}=-\frac{\partial p}{\partial x_i}+\frac{\partial}{\partial x_j}\left[\mu\left(\frac{\partial u_i}{\partial x_j}+\frac{\partial u_j}{\partial x_i}\right)\right]-2\varepsilon_{ijk}\Omega_j u_k-\varepsilon_{imk}\varepsilon_{kjn}\Omega_m x_n\,, \tag{2}$$

where ε_{ijk} is the alternating or permutation symbol.

For compressible flows, a simple adiabatic energy equation is used to get the local temperature. The equation is written as

$$h+\frac{u_i u_i}{2}-\frac{U^2}{2}=\text{constant}, \tag{3}$$

where h is enthalpy and U is the local wheel speed. The density is calculated using the state equation.

In equation (2) the effective viscosity μ is equal to the sum of laminar viscosity μ_l and eddy viscosity μ_t. The eddy viscosity μ_t is determined through the relation

$$\mu_t=C_\mu\rho\frac{k^2}{\varepsilon}, \tag{4}$$

where the turbulence kinetic energy k and the turbulence energy dissipation rate ε are calculated using the turbulence k–ε equations

$$\frac{\partial}{\partial x_j}(\rho u_j k)=\frac{\partial}{\partial x_j}\left(\frac{\mu}{\sigma_k}\frac{\partial k}{\partial x_j}\right)+G-\rho\varepsilon\,, \tag{5}$$

$$\frac{\partial}{\partial x_j}(\rho u_j \varepsilon)=\frac{\partial}{\partial x_j}\left(\frac{\mu}{\sigma_\varepsilon}\frac{\partial \varepsilon}{\partial x_j}\right)+C_1 G\frac{\varepsilon}{k}-C_2\rho\frac{\varepsilon^2}{k}. \tag{6}$$

Here G is the production rate of turbulence kinetic energy. Even though several modified turbulence k–ε models for rotating flows have been proposed, the authors found that the regular k–ε model worked as well as the modified models.[11] Thus the regular k–ε model is still applied here. The coefficient values of the k–ε turbulence model employed in the present work are shown below.[17,18]

C_μ	C_1	C_2	σ_k	σ_ε	κ	E
0·09	1·44	1·92	1·0	1·3	0·4187	9·0

To facilitate co-ordinate transformations, the transport equations (2), (5) and (6) can also be written in a general form, for an arbitrary variable ϕ, as

$$\frac{\partial}{\partial x_j}(\rho\phi u_j)=\frac{\partial}{\partial x_j}\left(\Gamma_\phi\frac{\partial\phi}{\partial x_j}\right)+s_\phi. \tag{7}$$

GENERAL CO-ORDINATES

In the present work a general co-ordinate system, i.e. a body-fitted co-ordinate system, is used to handle the complex geometries of most rotating flows. Governing equations can be transformed into curvilinear co-ordinates according to a general transformation

$$\xi^i=\xi^i(x_1, x_2, x_3), \tag{8}$$

where the ξ^i's represent general co-ordinates.

Using standard transformation formulae, the transport equation (7) can be expressed as

$$\frac{\partial}{\partial\xi^1}\left(\rho U_1\phi-J\Gamma_\phi\frac{\partial\phi}{\partial\xi^1}A_{11}\right)+\frac{\partial}{\partial\xi^2}\left(\rho U_2\phi-J\Gamma_\phi\frac{\partial\phi}{\partial\xi^2}A_{22}\right)+\frac{\partial}{\partial\xi^3}\left(\rho U_3\phi-J\Gamma_\phi\frac{\partial\phi}{\partial\xi^3}A_{33}\right)=s^\phi+Js_\phi, \tag{9}$$

where the extra source term s^ϕ comes from non-orthogonal co-ordinate systems, the scaled contravariant velocity components are defined as

$$U_i=J\left(u_j\frac{\partial\xi^i}{\partial x_j}\right), \tag{10}$$

and the coefficients A_{ij} are written as

$$A_{ij}=\frac{\partial\xi^i}{\partial x_k}\frac{\partial\xi^j}{\partial x_k}. \tag{11}$$

The continuity equation becomes

$$\frac{\partial}{\partial\xi^j}(\rho U_j)=0. \tag{12}$$

Many internal flows have a predominant flow direction, along which diffusion terms are very small and negligible in comparison to convection terms. The general transport equation (9) can be parabolized in the predominant flow direction by neglecting the diffusion terms in that direction. It is much easier to solve the parabolized equations than the full Navier–Stokes equations because a 'one-way' co-ordinate appears in the predominant flow direction, and a space-marching technique can be used to sweep through a three-dimensional flow field using two-dimensional computer storage.

DISCRETIZATION

A finite-volume formulation is applied to obtain the discretized equations, which express the conservation principle for a control volume. The general transport equation (9) is integrated over a control volume, and piecewise profiles are used to evaluate the integrals. The power-law differencing scheme[19] is selected to approximate the values on the control volume faces in terms of nodal values, so that the discretized equations have the following form:

$$A_P\phi_P = A_N\phi_N + A_S\phi_S + A_E\phi_E + A_W\phi_W + A_D\phi_D + A_U\phi_U + (s^\phi + Js_\phi)\Delta\xi^1\Delta\xi^2\Delta\xi^3. \tag{13}$$

Here P represents the grid point, which has the grid points N, S, E, W, D (downstream) and U (upstream) as its neighbors.

PRESSURE-BASED NUMERICAL METHOD FOR THREE-DIMENSIONAL ROTATING FLOWS

Physically, rotation has a significant impact on the flows inside turbomachinery components. This should be reflected mathematically, which means that the numerical procedures used to simulate the flow fields should take into account the influence of rotation on the computations. In the present study, the basic idea of the pressure based numerical method will be applied to rotating flows so that a new numerical procedure will be developed, which does consider the effect of rotation on numerical computations.

Pressure correction

Comparing equations (2) and (9) with equation (13), we can write the discretized momentum equations as

$$\begin{bmatrix} A_P & 0 & 0 \\ 0 & A_P & 0 \\ 0 & 0 & A_P \end{bmatrix}\begin{Bmatrix} u_1 \\ u_2 \\ u_3 \end{Bmatrix} = \sum A_i \begin{Bmatrix} u_1 \\ u_2 \\ u_3 \end{Bmatrix} + \begin{Bmatrix} S^1 \\ S^2 \\ S^3 \end{Bmatrix}\Delta\xi^1\Delta\xi^2\Delta\xi^3 - \begin{Bmatrix} p_{x_1} \\ p_{x_2} \\ p_{x_3} \end{Bmatrix} J\Delta\xi^1\Delta\xi^2\Delta\xi^3$$

$$- \begin{bmatrix} 0 & -2\Omega_3 & 2\Omega_2 \\ 2\Omega_3 & 0 & -2\Omega_1 \\ -2\Omega_2 & 2\Omega_1 & 0 \end{bmatrix}\begin{Bmatrix} u_1 \\ u_2 \\ u_3 \end{Bmatrix} J\Delta\xi^1\Delta\xi^2\Delta\xi^3, \tag{14}$$

where the source term S^i's can be expressed as

$$S^i = s^i - J\varepsilon_{imk}\varepsilon_{kjn}\Omega_m\Omega_j x_n, \tag{15}$$

and the s^i's are defined by the s^ϕ in equation (9).

Based on the estimated pressure field p^*, equation (14) can be solved and the resulting velocity field does satisfy the momentum equation

$$\begin{bmatrix} A_P & 0 & 0 \\ 0 & A_P & 0 \\ 0 & 0 & A_P \end{bmatrix}\begin{Bmatrix} u_1 \\ u_2 \\ u_3 \end{Bmatrix}^* = \sum A_i \begin{Bmatrix} u_1 \\ u_2 \\ u_3 \end{Bmatrix}^* + \begin{Bmatrix} S^1 \\ S^2 \\ S^3 \end{Bmatrix}\Delta\xi^1\Delta\xi^2\Delta\xi^3 - \begin{Bmatrix} p_{x_1} \\ p_{x_2} \\ p_{x_3} \end{Bmatrix}^* J\Delta\xi^1\Delta\xi^2\Delta\xi^3$$

$$- \begin{bmatrix} 0 & -2\Omega_3 & 2\Omega_2 \\ 2\Omega_3 & 0 & -2\Omega_1 \\ -2\Omega_2 & 2\Omega_1 & 0 \end{bmatrix}\begin{Bmatrix} u_1 \\ u_2 \\ u_3 \end{Bmatrix}^* J\Delta\xi^1\Delta\xi^2\Delta\xi^3. \tag{16}$$

The partial derivatives of pressure are transformed to curvilinear co-ordinates as

$$\begin{Bmatrix} p_{x_1} \\ p_{x_2} \\ p_{x_3} \end{Bmatrix} = \begin{bmatrix} \xi^1_{x_1} & \xi^2_{x_1} & \xi^3_{x_1} \\ \xi^1_{x_2} & \xi^2_{x_2} & \xi^3_{x_2} \\ \xi^1_{x_3} & \xi^2_{x_3} & \xi^3_{x_3} \end{bmatrix} \begin{Bmatrix} p_{\xi^1} \\ p_{\xi^2} \\ p_{\xi^3} \end{Bmatrix}. \tag{17}$$

In order to improve the estimated pressure p^* so that the resulting velocity field satisfies the continuity equation, the pressure correction p' is assumed to have the form

$$p = p^* + p'. \tag{18}$$

Then the corresponding velocity corrections can be obtained in a similar manner, i.e.

$$\begin{Bmatrix} u_1 \\ u_2 \\ u_3 \end{Bmatrix} = \begin{Bmatrix} u_1 \\ u_2 \\ u_3 \end{Bmatrix}^* + \begin{Bmatrix} u_1 \\ u_2 \\ u_3 \end{Bmatrix}'. \tag{19}$$

Inserting equations (17)–(19) into equation (14) and comparing it with equation (16), we get

$$\begin{Bmatrix} u_1 \\ u_2 \\ u_3 \end{Bmatrix} = \begin{Bmatrix} u_1 \\ u_2 \\ u_3 \end{Bmatrix}^* + \mathbf{P} \begin{Bmatrix} p_{\xi^1} \\ p_{\xi^2} \\ p_{\xi^3} \end{Bmatrix}' - \mathbf{E} \begin{Bmatrix} u_1 \\ u_2 \\ u_3 \end{Bmatrix}', \tag{20}$$

where

$$\mathbf{P} = \begin{bmatrix} B^1 & C^1 & D^1 \\ B^2 & C^2 & D^2 \\ B^3 & C^3 & D^3 \end{bmatrix},$$

$$\mathbf{E} = \frac{2J\,\Delta\xi^1\,\Delta\xi^2\,\Delta\xi^3}{A_P} \begin{bmatrix} 0 & -\Omega_3 & \Omega_2 \\ \Omega_3 & 0 & -\Omega_1 \\ -\Omega_2 & \Omega_1 & 0 \end{bmatrix},$$

$$B^i = -J \frac{\partial \xi^1}{\partial x_i} \Delta\xi^1\,\Delta\xi^2\,\Delta\xi^3 / A_P, \tag{21}$$

$$C^i = -J \frac{\partial \xi^2}{\partial x_i} \Delta\xi^1\,\Delta\xi^2\,\Delta\xi^3 / A_P,$$

$$D^i = -J \frac{\partial \xi^3}{\partial x_i} \Delta\xi^1\,\Delta\xi^2\,\Delta\xi^3 / A_P.$$

Substituting equation (19) into equation (20), we obtain the expressions for velocity corrections as

$$\begin{Bmatrix} u_1 \\ u_2 \\ u_3 \end{Bmatrix}' = (\mathbf{I} + \mathbf{E})^{-1} \mathbf{P} \begin{Bmatrix} p_{\xi^1} \\ p_{\xi^2} \\ p_{\xi^3} \end{Bmatrix}'. \tag{22}$$

The relationship between the Cartesian components and the scaled contravariant components can be written in a matrix form as

$$\begin{Bmatrix} U_1 \\ U_2 \\ U_3 \end{Bmatrix} = \mathbf{V} \begin{Bmatrix} u_1 \\ u_2 \\ u_3 \end{Bmatrix}, \tag{23}$$

where

$$\mathbf{V}=J\begin{bmatrix}\xi^1_{x_1} & \xi^1_{x_1} & \xi^1_{x_1}\\ \xi^2_{x_2} & \xi^2_{x_2} & \xi^2_{x_2}\\ \xi^3_{x_3} & \xi^3_{x_3} & \xi^3_{x_3}\end{bmatrix}. \tag{24}$$

Substituting equations (20) and (22) into equation (23), we obtain the expressions for the scaled contravariant velocity components as

$$\begin{Bmatrix}U_1\\U_2\\U_3\end{Bmatrix}=\begin{Bmatrix}U_1\\U_2\\U_3\end{Bmatrix}^* +\mathbf{V}(\mathbf{I}+\mathbf{E})^{-1}\mathbf{P}\begin{Bmatrix}p_{\xi^1}\\p_{\xi^2}\\p_{\xi^3}\end{Bmatrix}'. \tag{25}$$

Therefore, the relationship between the corrections of the scaled contravariant velocity components and pressure is expressed as follows:

$$\begin{Bmatrix}U_1\\U_2\\U_3\end{Bmatrix}'=\mathbf{V}(\mathbf{I}+\mathbf{E})^{-1}\mathbf{P}\begin{Bmatrix}p_{\xi^1}\\p_{\xi^2}\\p_{\xi^3}\end{Bmatrix}'. \tag{26}$$

After some algebraic operations, we can get the expression for the coefficient matrix,

$$\mathbf{V}(\mathbf{I}+\mathbf{E})^{-1}\mathbf{P}=\frac{J}{M}\begin{bmatrix}\dfrac{\partial\xi^1}{\partial x_j}M_{ij}B^i & \dfrac{\partial\xi^1}{\partial x_j}M_{ij}C^i & \dfrac{\partial\xi^1}{\partial x_j}M_{ij}D^i\\ \dfrac{\partial\xi^2}{\partial x_j}M_{ij}B^i & \dfrac{\partial\xi^2}{\partial x_j}M_{ij}C^i & \dfrac{\partial\xi^2}{\partial x_j}M_{ij}D^i\\ \dfrac{\partial\xi^3}{\partial x_j}M_{ij}B^i & \dfrac{\partial\xi^3}{\partial x_j}M_{ij}C^i & \dfrac{\partial\xi^3}{\partial x_j}M_{ij}D^i\end{bmatrix}, \tag{27}$$

where

$$\begin{aligned}
M &= 1+E_{12}^2+E_{13}^2+E_{23}^2,\\
M_{11}&=1+E_{23}^2,\\
M_{12}&=E_{12}-E_{13}E_{23},\\
M_{13}&=E_{12}E_{23}-E_{13},\\
M_{21}&=-E_{12}-E_{13}E_{23},\\
M_{22}&=1+E_{13}^2,\\
M_{23}&=E_{23}-E_{12}E_{13},\\
M_{31}&=E_{12}E_{23}-E_{13},\\
M_{32}&=-E_{23}-E_{12}E_{13},\\
M_{33}&=1+E_{12}^2,
\end{aligned} \tag{28}$$

and

$$\begin{aligned}
E_{12}&=-2J\Omega_3\,\Delta\xi^1\,\Delta\xi^2\,\Delta\xi^3/A_{\mathrm{P}},\\
E_{13}&=2J\Omega_2\,\Delta\xi^1\,\Delta\xi^2\,\Delta\xi^3/A_{\mathrm{P}},\\
E_{23}&=-2J\Omega_1\,\Delta\xi^1\,\Delta\xi^2\,\Delta\xi^3/A_{\mathrm{P}}.
\end{aligned} \tag{29}$$

If near-orthogonal co-ordinates are used, off-diagonal terms are so small compared with diagonal pressure gradient terms that they can be neglected. The approximate expression for equation (27) can be written as

$$\mathbf{V}(\mathbf{I}+\mathbf{E})^{-1}\mathbf{P}=\frac{J}{M}\begin{bmatrix}\dfrac{\partial\xi^1}{\partial x_j}M_{ij}B^i & 0 & 0\\ 0 & \dfrac{\partial\xi^2}{\partial x_j}M_{ij}C^i & 0\\ 0 & 0 & \dfrac{\partial\xi^3}{\partial x_j}M_{ij}D^i\end{bmatrix}. \tag{30}$$

For $\mathbf{E}=0$ this reduces to the usual equations relating velocity corrections to pressure changes, but for $\mathbf{E}\neq 0$ it means that the Coriolis terms are included directly in the pressure correction, not explicitly as they would be if made source terms.

The expression given by equation (30) must be used with the global and local continuity conditions to correct the pressure. First the global average pressure correction is discussed.

Global average pressure correction. The global continuity condition,

$$M_{\text{in}}=\sum \rho U_3\,\Delta\xi^1\,\Delta\xi^2, \tag{31}$$

is employed to obtain the average pressure correction on the current cross-stream plane. Here the ξ^3 direction is assumed to be aligned with the throughflow direction. By inserting the expression coming from equations (25) and (30), i.e.

$$U_3=U_3^*+\frac{J}{M}\frac{\partial\xi^3}{\partial x_j}M_{ij}D^i p'_{\xi^3}, \tag{32}$$

into equation (31), the average pressure gradient can be determined,

$$\bar{p}'_{\xi^3}=\frac{M_{\text{in}}-\sum \rho U_3^*\,\Delta\xi^1\,\Delta\xi^2}{\sum \rho\dfrac{J}{M}\dfrac{\partial\xi^3}{\partial x_j}M_{ij}D^i\,\Delta\xi^1\,\Delta\xi^2}. \tag{33}$$

The global pressure correction is first conducted to accelerate the establishment of the correct pressure field. Then the continuity equation is used to obtain the pressure correction equation locally.

Local pressure correction. By integrating the continuity equation (12) over a control volume, the local continuity condition can be written as

$$\iint_S \rho\{\mathrm{d}\xi^2\,\mathrm{d}\xi^3,\ \mathrm{d}\xi^3\,\mathrm{d}\xi^1,\ \mathrm{d}\xi^1\,\mathrm{d}\xi^2\}\begin{Bmatrix}U_1\\U_2\\U_3\end{Bmatrix}=0. \tag{34}$$

By substituting equation (25) into equation (34), the above continuity condition is written with the pressure correction as

$$\iint_S \rho\{\mathrm{d}\xi^2\,\mathrm{d}\xi^3,\ \mathrm{d}\xi^3\,\mathrm{d}\xi^1,\ \mathrm{d}\xi^1\,\mathrm{d}\xi^2\}\,\mathbf{V}(\mathbf{I}+\mathbf{E})^{-1}\mathbf{P}\begin{Bmatrix}p_{\xi^1}\\p_{\xi^2}\\p_{\xi^3}\end{Bmatrix}'=-m_p, \tag{35}$$

where

$$m_p = \iint_S \rho \{d\xi^2\, d\xi^3, d\xi^3\, d\xi^1, d\xi^1\, d\xi^2\} \begin{Bmatrix} U_1 \\ U_2 \\ U_3 \end{Bmatrix}^* . \tag{36}$$

The central differencing scheme is used to discretize equation (35) so that the resulting equation, i.e. the pressure correction equation, can be expressed as

$$A_P p'_P = A_N p'_N + A_S p'_S + A_E p'_E + A_W p'_W + A_D p'_D + A_U p'_U + s_P, \tag{37}$$

where

$$\begin{aligned} A_{N\,or\,S} &= \left[\frac{\rho J}{M \Delta\xi^1} \frac{\partial \xi^1}{\partial x_j} M_{ij} B^i \Delta\xi^2 \Delta\xi^3 \right]_{n\,or\,s}, \\ A_{E\,or\,W} &= \left[\frac{\rho J}{M \Delta\xi^2} \frac{\partial \xi^2}{\partial x_j} M_{ij} C^i \Delta\xi^3 \Delta\xi^1 \right]_{e\,or\,w}, \\ A_{D\,or\,U} &= \left[\frac{\rho J}{M \Delta\xi^3} \frac{\partial \xi^3}{\partial x_j} M_{ij} D^i \Delta\xi^1 \Delta\xi^2 \right]_{d\,or\,u}, \\ A_P &= A_N + A_S + A_E + A_W + A_D + A_U, \end{aligned} \tag{38}$$

and

$$s_P = [(\rho U_1^*)_n - (\rho U_1^*)_s] \Delta\xi^2 \Delta\xi^3 + [(\rho U_2^*)_e - (\rho U_2^*)_w] \Delta\xi^3 \Delta\xi^1 + [(\rho U_3^*)_d - (\rho U_3^*)_u] \Delta\xi^1 \Delta\xi^2 + \tilde{s}_P,$$

where the source term $\tilde{s}_P = 0$ if the off-diagonal pressure gradient terms are neglected.

During the space-marching process the two-dimensional form of the pressure correction equation is used, which is derived simply by assuming that $p'_D = p'_U = 0$. For purely parabolic flows the justification for this assumption is obvious: the upstream pressure P_U is known and thus $P'_U = 0$, while the downstream pressure P_D has no upstream impact ($P'_D = 0$). For flows which are only partially parabolic, such as those in strongly curved ducts and turbine cascades, a three-dimensional elliptic pressure correction is carried out after a complete forward marching pass by solving equation (38) with the updated local mass imbalance.

Numerical solution sequence

Since the parabolized Navier–Stokes equations are dealt with, a space-marching method is an appropriate choice to use. The numerical solution sequence is described as follows:

(1) Velocities are obtained by solving the momentum equation (14), using an approximate pressure field from an initial guess or a previous iteration.
(2) The global pressure correction is performed using equation (33). The two-dimensional form of the pressure correction equation (37) obtained from the local continuity condition is solved to correct the pressure field. Subsequently velocities are adjusted using equation (26).
(3) For compressible and turbulent flows, scalar variables such as T, ρ, k and ε are determined.
(4) Steps 1–3 are repeated until satisfactory convergence is achieved. Here, the ratio of the sum of mass residuals and inlet mass flow rate is used as the convergence criterion.
(5) Shift to next downstream plane and repeat steps 1–4 until a forward marching sweep is completed.

Since the present study focuses on the development of the pressure-based method for 3D rotating flows, the single-pass, space-marching procedure described above is applied to the numerical computations. Also, the 'flare' approach[20] is used to take care of possible reverse flows in the throughflow direction.

Computational arrangements and boundary conditions

A non-staggered variable arrangement is utilized to minimize the amount of geometrical information required to be stored. For the finite-volume approach, it is necessary to evaluate velocity components at cell faces. In early unsuccessful attempts to use non-staggered variable arrangements, linear interpolation was used to approximate these face values and this led to pressure oscillations. In the present work, a special interpolation scheme proposed by Rhie and Chow[21] is used to overcome the difficulty. The interpolation scheme was described by Peric[13] as follows: to evaluate a velocity component at a cell face, interpolate using the discretized momentum equation (13) for the two neighbouring nodes. Instead of interpolating the pressure gradients, use a pressure gradient centred about the cell face. In this manner a five-point form for the pressure equation is obtained.

In the present work, a grid mesh is arranged so that the mesh defines the control volume boundaries and the computational nodes are then put in the centre of each control volume. The main advantage of this arrangement is that it is much easier to treat different types of boundary conditions. For example, the approximate boundary condition for pressure is no longer necessary.

In the case of turbulent flows calculation of the stresses on the walls needs special attention, since the k–ε turbulence models apply only to fully turbulent flows and near no-slip walls the flow is not fully turbulent. Due to the existence of boundary layers, across which steep variations of flow properties occur, the standard k–ε turbulence models become inadequate. Here, the 'wall function' approach[17] is applied to bridge the regions. The expressions for wall shear stress as well as boundary conditions for k and ε are the same as those given in Reference 11.

NUMERICAL COMPUTATIONS

Three-dimensional numerical simulations of rotating flows have been conducted using the procedure just discussed and compared with two different sets of experimental data. Among

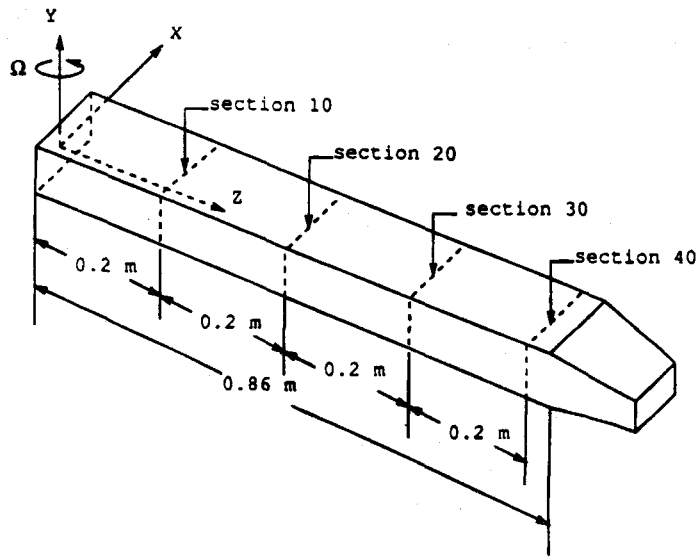

Figure 1. Wagner's 3D channel

them, the data of Wagner and Velkoff[16] were taken in a geometrically simple apparatus, while Eckardt's data[14,15] came from a centrifugal impeller which was geometrically complicated.

Three-dimensional channel flow

Wagner and Velkoff[16] designed the testing apparatus (Figure 1) to study the secondary flows in a rotating radial channel. The test section was mounted on a rotating horizontal table. The channel, using air as the working medium, was 0·864 m in length with a contracting section at the exit to minimize the exit-flow effect. The rectangular cross section had a height (h) of 0·0445 m and a width (b) of 0·121 m. A flow velocity (W_m) of about 15·3 m s^{-1} was chosen to achieve the desired Reynolds number ($W_m h/\nu$) of 46 000. Wagner and Velkoff presented experimental results for five rotation numbers ($\Omega b/W_m = 0{\cdot}07, 0{\cdot}10, 0{\cdot}14, 0{\cdot}18$ and $0{\cdot}22$). The present study treated the flow as incompressible, and employed a 11×17 grid pattern in the cross-stream direction with 45 steps downstream starting from the duct entrance where a uniform streamwise velocity was assumed without secondary velocity. Grid lines are clustered near the entrance and the walls by using Roberts' stretching functions[22] in order to resolve the rapid variation of physical variables such as velocity.

For rotation numbers 0·07 and 0·22 ($\Omega = 100$ and 300 rpm), the data of Wagner and Velkoff[16] were compared at 0·65 m (cross section 32) from the entrance with predicted streamwise velocities at the horizontal centreline. As seen in Figure 2, the numerical predictions were satisfactory.

The predicted cross-stream velocities at the horizontal centreline at 0·73 m (cross section 36) from the entrance are compared with the measured data for rotation speeds of 100 and 300 rpm in Figure 3. As can be seen, the numerical simulations yielded reasonably good agreement with the experiment. It is quite apparent that the cross-stream velocity components increase linearly with rotation, and the proportionality factor is about $100/\Omega$.[16] In order to visualize the secondary flow pattern, the predicted cross-stream velocity vector fields at 0·24 and 0·73 m (cross sections 12 and 36) were plotted in Figure 4 for rotation speeds of 100 and 300 rpm. They showed the presence of two similar longitudinal vortices, one in the upper half and the other in the lower half of the cross section. A qualitative comparison of predicted secondary velocity vectors and experimental ones is given in Figure 5, which shows that the prediction gave a better description of secondary flow than the measurements taken by Wagner and Velkoff. Finally, the three-dimensional velocity fields at cross sections 12 and 36 visualized in Figure 6 for rotation speeds of 100 and 300 rpm.

Eckardt's centrifugal impeller

This section describes the application of the present method to turbulent air flow in a radial discharge impeller (Figure 7), which was studied experimentally by Eckardt.[14-15] The impeller was run at design point operating conditions defined as rotational speed = 14 000 rpm and flow rate = 5·31 kg s^{-1}. In this case, the Reynolds number $Re = 5{\cdot}3 \times 10^5$ and the rotation number $R_0 = 1{\cdot}77$.

The compressible flow computation was carried out on the single blade channel shown schematically in Figure 7. Detailed information on the impeller geometry can be found in Reference 23. A constant area annular section was added upstream of the impeller so that uniform boundary conditions could be specified at the inlet. Periodic boundary conditions were also applied to this section. There were 15 grid points in the circumferential direction, 15 grid points in the spanwise direction, and 130 grid points in the throughflow direction. Three of the 15 grid points were located inside the top clearance between the blade tip and the shroud surface. A stretching transformation[22] was used to have coarse grid spacings near pressure and hub sides and fine grid spacings near suction and shroud sides. The reason for employing such a mesh

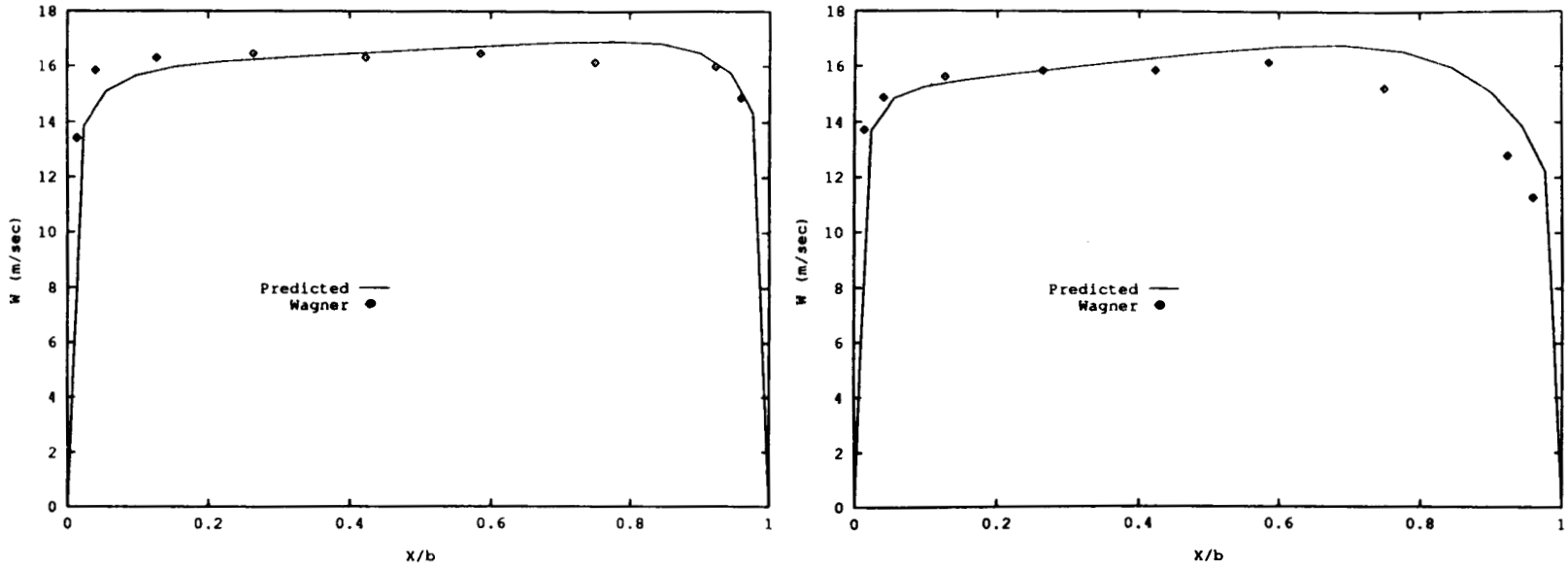

Figure 2. Comparison of predicted and experimental streamwise velocity profiles at section 32. (Left) 100 rpm. (Right) 300 rpm

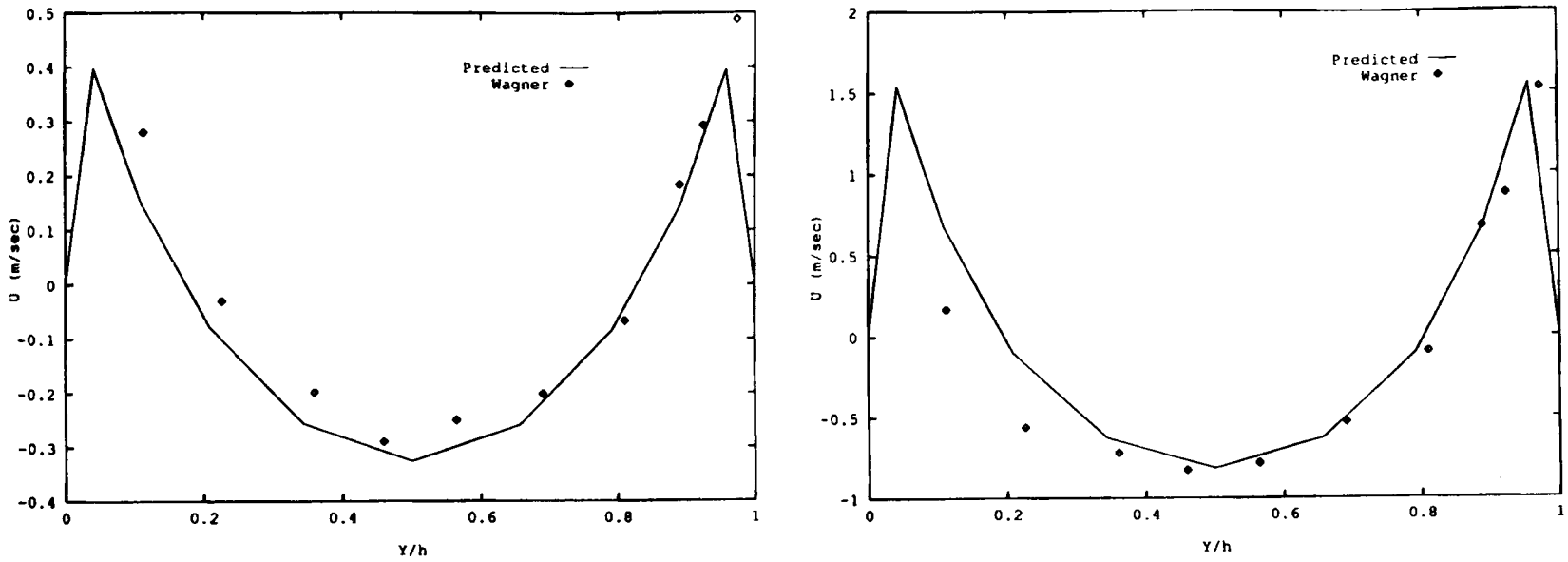

Figure 3. Comparison of predicted and experimental cross-flow velocity profile at section 36. (Left) 100 rpm. (Right) 300 rpm

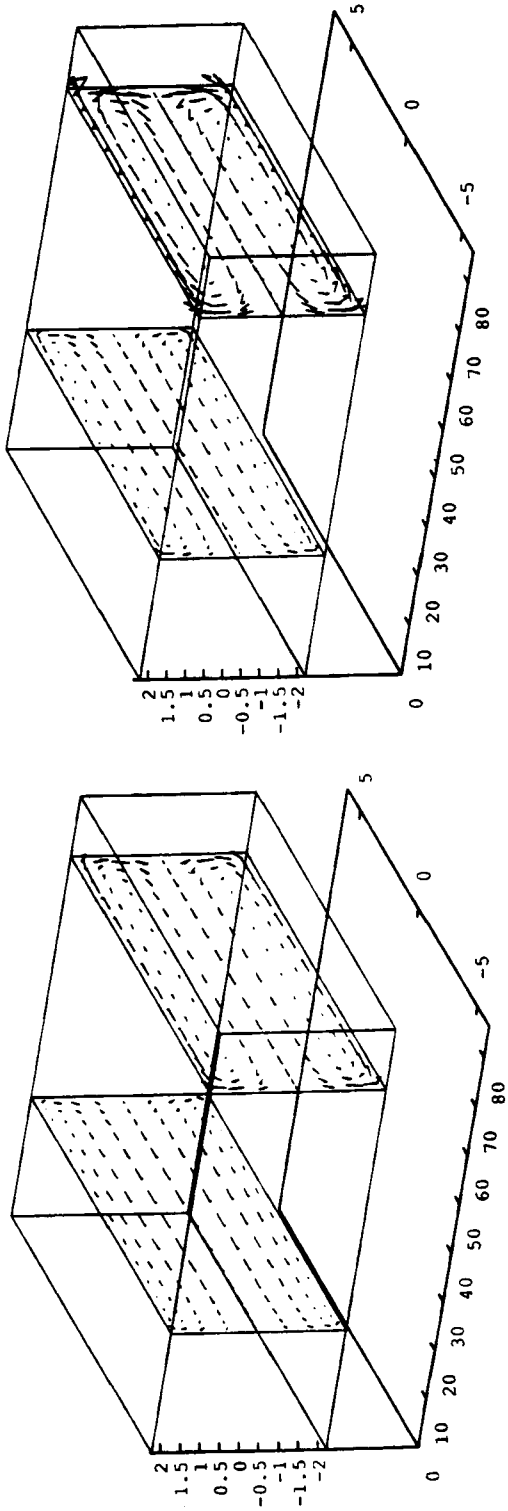

Figure 4. Secondary velocity vector fields at sections 12 and 36. (Left) 100 rpm. (Right) 300 rpm

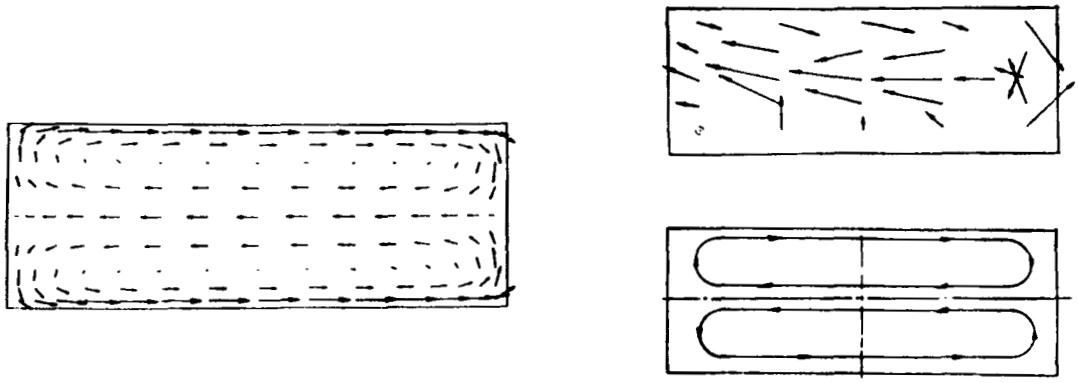

Figure 5. Qualitative comparison of predicted and experimental secondary flows. (Left) predicted secondary flow at section 36, $\Omega = 300$ rpm. (Right) Wagner's experimental data and sketch

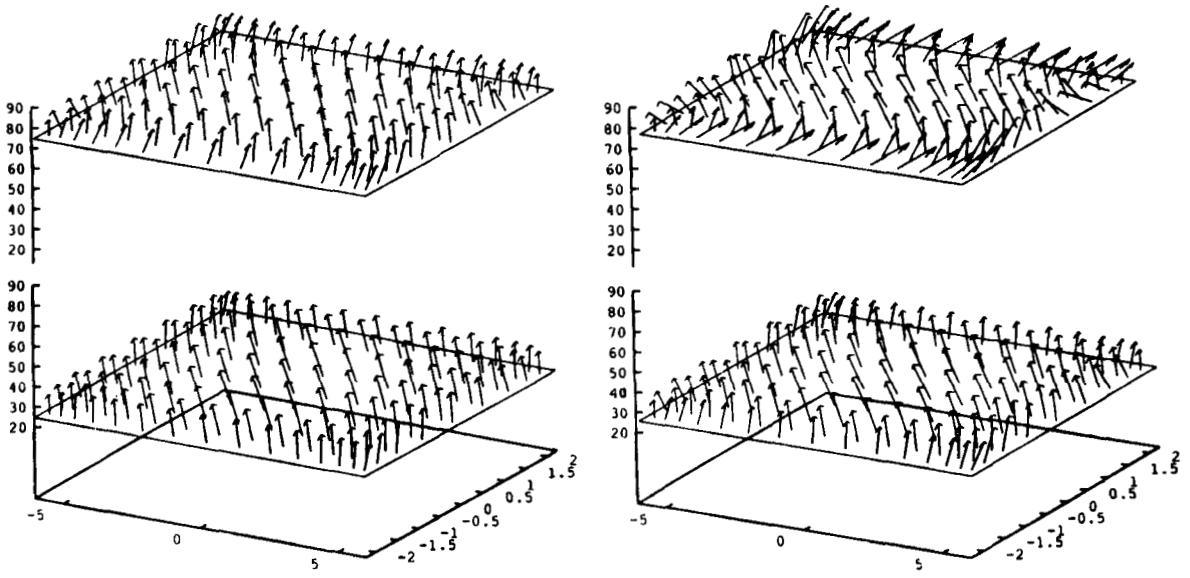

Figure 6. Predicted velocity vectors at sections 12 and 36. (Left) 100 rpm. (Right) 300 rpm

arrangement is that the velocity distributions obtained by Eckardt[15] showed potential flow character in the part of the flow field from mid-passage to hub.[23] The region near the pressure side showed a more gradual increase in velocity away from the surface. In the present work, the wall-function method was used to handle solid walls. The first requirement when using the wall-function method is that the grid points adjacent to the walls have to be sufficiently remote from the walls so that the viscous effects are entirely overwhelmed by the turbulent ones. Having coarse grid spacings helps to put the grid points out of the viscous sublayer.

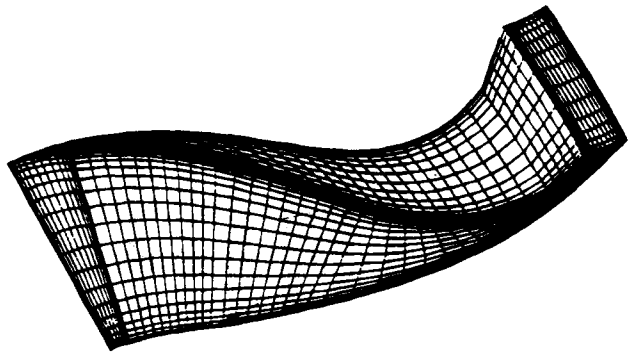

Figure 7. The geometry and grid of an Eckardt's impeller channel

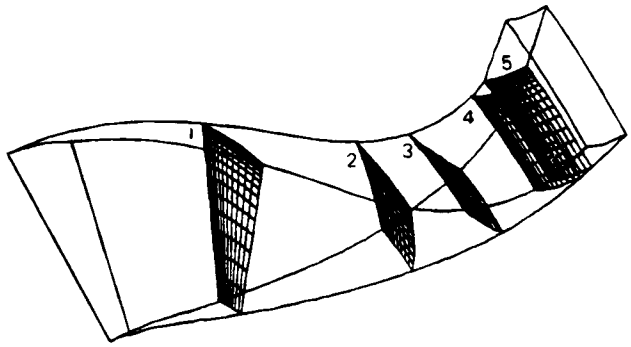

Figure 8. The cross section planes where the velocity is visualized and compared with Eckardt's data

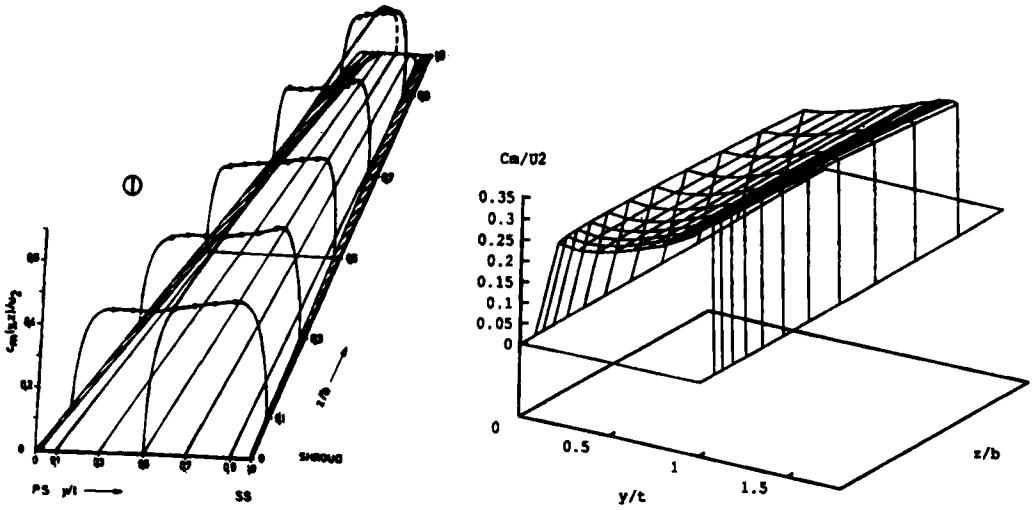

Figure 9. Velocity distribution at measurement area 1. (Left) Eckardt's data. (Right) Predicted result

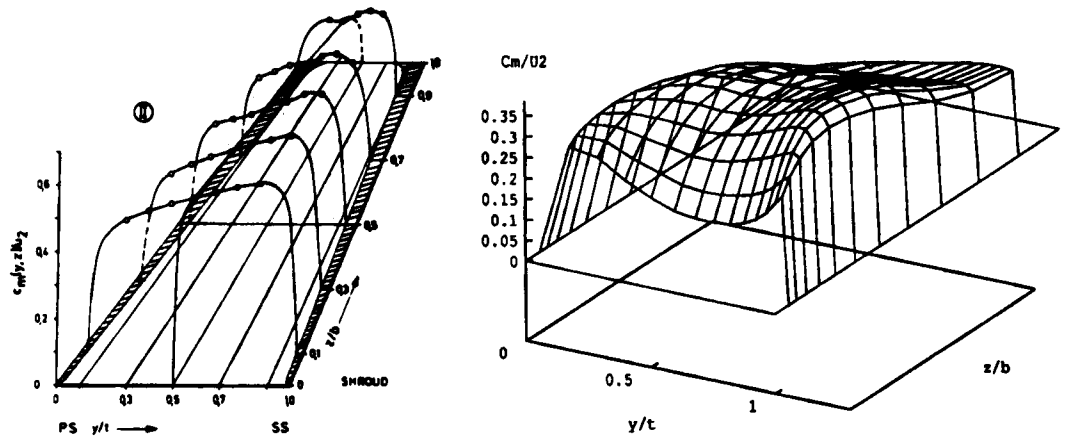

Figure 10. Velocity distribution at measurement area 2. (Left) Eckardt's data. (Right) Predicted result

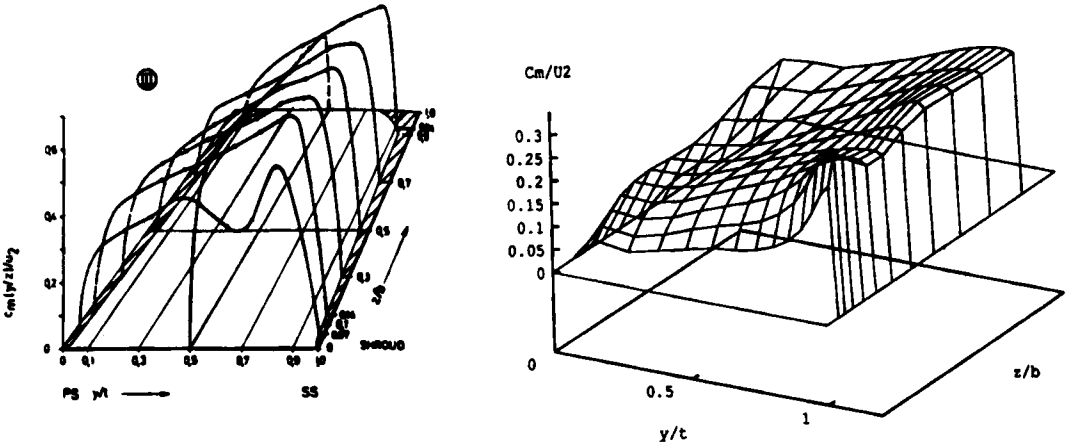

Figure 11. Velocity distribution at measurement area 3. (Left) Eckardt's data. (Right) Predicted result

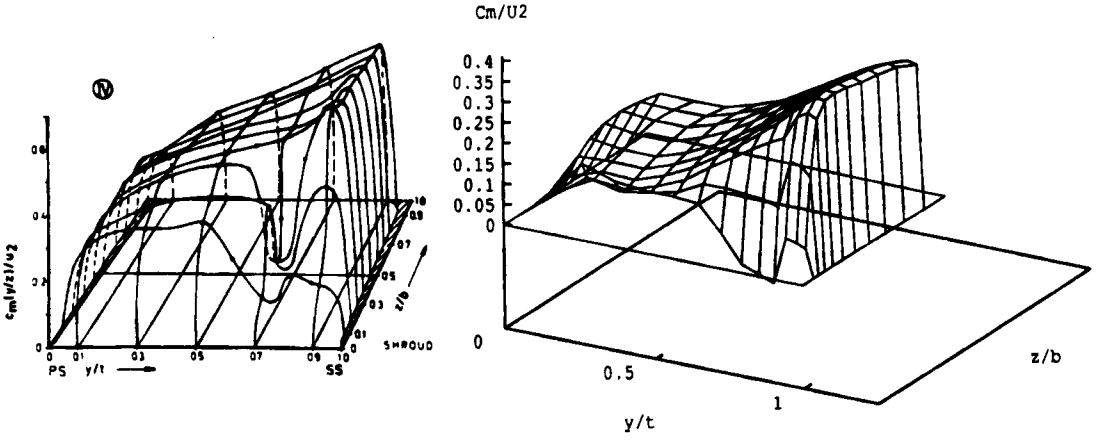

Figure 12. Velocity distribution at measurement area 4. (Left) Eckardt's data. (Right) Predicted result

The predicted results were compared with the intra-blade-row velocity and shroud surface pressure distribution taken by Eckardt. The velocity fields were visualized and compared on surfaces 1–5 (see Figure 8).

Comparisons of the predicted primary velocity profiles with the experimental data at the five surfaces are given in Figures 9–13. The numerical data have been plotted in the same format used by Eckardt. Reasonably good agreement is shown at all locations. Figures 9 and 10 show that the simulated flow, as compared with the experimental data, is also regular at a comparatively low blade loading and preserves its potential character. From the predicted velocity profiles at surface 2 (Figure 10), a little velocity distortion can be observed in a small area near the shroud surface where no experimental data were available.

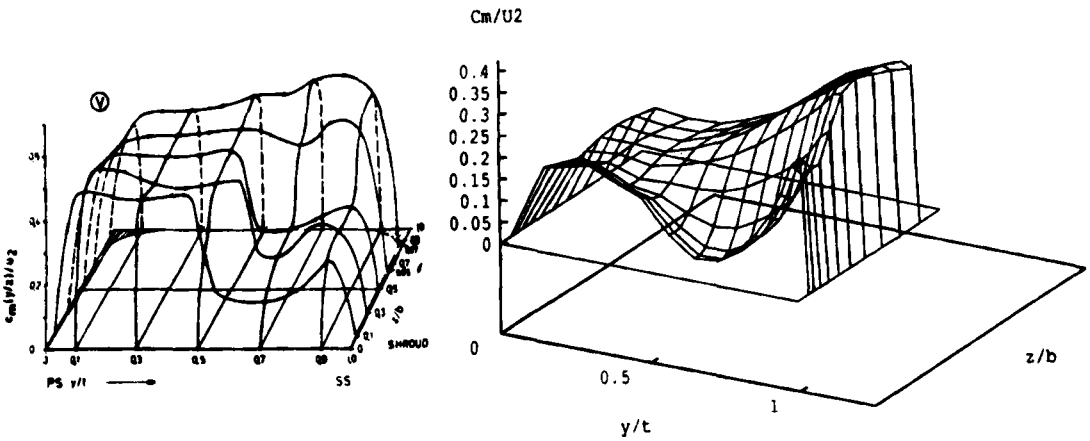

Figure 13. Velocity distribution at measurement area 5. (Left) Eckardt's data. (Right) Predicted result

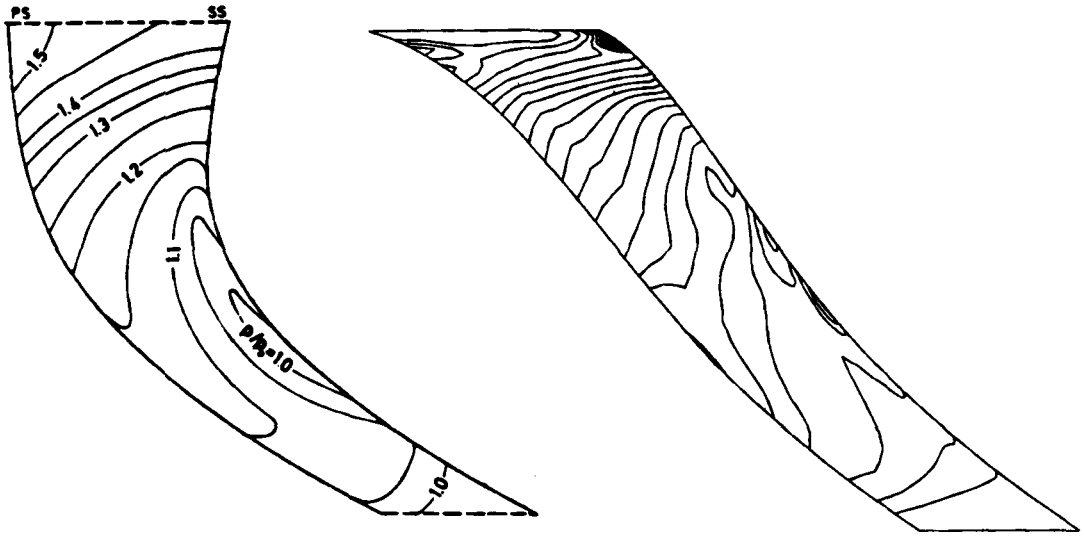

Figure 14. Pressure contours along the shroud surface. (Left) Eckardt's data. (Right) Predicted result

Both predicted and experimental results show that the velocity distortions of the impeller flow pattern start to appear near the shroud surface a short distance downstream at surface 3 (Figure 11). In the rest of the flow field, the potential flow pattern appears to be preserved.

The velocity distortions rapidly enlarge downstream and develop into jet/wake flow patterns, as shown in Figures 12 and 13 for surfaces 4 and 5, respectively. The numerical computations successfully predicted the wake regions at two surfaces, and gave results which were comparable with the experimental data.

The predicted and measured pressure contours along the shroud surface are presented and compared in Figure 14. The comparison looks reasonably good.

CONCLUSION

A new pressure-based numerical method for three-dimensional viscous rotating flows has been developed and presented. The parabolized Navier–Stokes equations are solved with a space-marching technique, and body-fitted curvilinear co-ordinate systems are employed to handle the general complexity of geometries which most rotating flows feature. The present method was applied to a rotating channel and a centrifugal impeller, and the numerical results showed reasonably good agreement with the experimental data. Both compressible and incompressible flows were treated successfully and rotation speeds as high as 14 000 rpm were readily handled. The characteristic secondary flows and jet/wake flow patterns were accurately simulated.

ACKNOWLEDGEMENT

This research has been supported by the Rotating Machinery and Controls (ROMAC) Industrial Research Group at the University of Virginia.

APPENDIX: NOMENCLATURE

A	coefficient in the finite-difference equations
G	production rate of turbulence kinetic energy
h	enthalpy
J	Jacobian of curvilinear transformation
k	turbulent kinetic energy
m_P	mass residual
R_0	rotation number
Re	Reynolds number
p	static pressure
s_ϕ	source term in a general transport equation
s^ϕ	source term coming from non-orthogonality
U	local wheel speed
u_i	Cartesian velocity components
U_i	scaled contravariant velocity components
x_i	Cartesian co-ordinate components
ε	turbulent energy dissipation
ε_{ijk}	alternating or permutation symbol
ρ	density
ϕ	an arbitrary variable
Ω	rotation speed

Ω_i	Cartesian components of rotation speed
μ_l	laminar viscosity
μ_t	$C_\mu \rho K^2/\varepsilon$, turbulent viscosity
μ	$\mu_l + \mu_t$, effective viscosity
Γ_ϕ	diffusion coefficient
ξ^i	curvilinear co-ordinate components
$\Delta\xi^i$	finite-difference mesh spacings

Subscripts

e, w, n, s, u, d	references to control volume faces
P, E, W, N, S, U, D	references to control point and neighboring grid points
i, j, k	Cartesian co-ordinate direction indices

Superscripts

*	current or guessed value
'	correction value
-	average value

REFERENCES

1. D. Japikse, 'REVIEW-progress in numerical turbomachinery analysis', *ASME J. Fluids Eng.*, **98**, 592–606 (1976).
2. D. Adler, 'Status of centrifugal impeller internal aerodynamics, Part 1: Inviscid flow prediction methods', *ASME J. Eng. Power*, **102**, 728–746 (1980).
3. W. D. McNally and P. M. Sockol, 'REVIEW-computational methods for internal flows with emphasis on turbomachinery', *ASME J. Fluids Eng.*, **107**, 6–22 (1985).
4. J. H. G. Howard, S. V. Patankar and R. M. Bordynuik, 'Flow prediction in rotating ducts using Coriolis-modified turbulence models', *ASME J. Fluids Eng.*, **102**, 456–461 (1980).
5. A. K. Majumdar, V. S. Pratap and D. B. Spalding, 'Numerical computation of flow in rotating ducts', *ASME J. Fluids Eng.*, **99**, 148–153 (1977).
6. A. K. Majumdar and D. B. Spalding, 'A numerical investigation of three-dimensional flows in a rotating duct by a partially parabolic procedure', *ASME Paper 77-WA/FE-7*, 1977.
7. F. Bansod and C. Rhie, 'Computation of flow through a centrifugal impeller with tip clearance', *AIAA Paper 90-2021*, 1990.
8. C. Hah and H. Krain, 'Secondary flows and vortex motions in a high efficiency backswept impeller at design and off design conditions', *J. Turbomach.*, **112**, 7–13 (1990).
9. J. Moore and J. G. Moore, '3D viscous calculations at design and off design conditions for the NASA 48 radial inlet centrifugal impeller', *Proc. 8th Int. Symp. on Air Breathing Engines*, Ohio (1987).
10. S. V. Patankar and D. B. Spalding, 'A calculation procedure for heat, mass and momentum transfer in three-dimensional parabolic flow', *Int. J. Heat Mass*, **15**, 1787–1805 (1972).
11. Q. Shi and R. J. Ribando, 'Numerical simulations of viscous rotating flows using a new pressure-based method', *Comput. Fluids*, **21**, 475–489 (1992).
12. C. M. Rhie, 'A three-dimensional passage flow analysis method aimed at centrifugal impellers', *Comput. Fluids*, **13**, 443–460 (1985).
13. M. Peric, 'A finite volume method for the prediction of three-dimensional fluid flow in complex ducts', *Ph.D. Dissertation*, Imperial College, London, 1985.
14. D. Eckardt, 'Instantaneous measurements in the jet-wake discharge flow of a centrifugal compressor impeller', *ASME J. Eng. Power*, **97**, 337–346 (1975).
15. D. Eckardt, 'Detailed flow investigations within a high-speed centrifugal compressor impeller', *ASME J. Fluids Eng.*, **98**, 390–402 (1976).
16. R. E. Wagner and H. R. Velkoff, 'Measurement of secondary flows in a rotating duct', *ASME J. Eng. Power*, **94**, 261–270 (1972).
17. B. E. Launder and D. B. Spalding, 'The numerical computation of turbulent flows', *Comput. Methods Appl. Mech. Eng.*, **3**, 269–289 (1974).
18. I. Demirdzic, A. D. Gosman, I. R. Issa and M. Peric, 'A calculation procedure for turbulent flow in complex geometries', *Comput. Fluids*, **15**, 251–273 (1987).
19. S. V. Patankar, *Numerical Heat Transfer and Fluid Flow*, Hemisphere, New York, 1980.

20. T. A. Reyhner and I. Flugge-Lotz, 'The interaction of a shock wave with a laminar boundary layer', *Int. J. Non-Linear Mech.*, **3**, 173–199 (1968).
21. C. M. Rhie and W. L. Chow, 'Numerical study of the turbulent flow past an airfoil with trailing edge separation', *AIAA J.*, **21**, 1525–1532 (1983).
22. G. O. Roberts, 'Computational meshes for boundary layer problems', *Proc. 2nd Int. Conf. Numerical Methods Fluid Dynamics, Lecture Notes in Physics* Vol. 8, Springer, New York, 1971, pp. 171–177.
23. P. Schuster and U. Schmidt-Eisenlohr, 'Flow field analysis of radial and backswept centrifugal compressor impellers, Part 2: Comparison of potential flow calculations and measurements', *ASME Paper in Performance Prediction of Centrifugal Pumps and Compressors*, 1980, pp. 87–95.